UNICA UNIVERSITÀ DEGLI STUDI DI CAGLIARI

This is the Author's accepted manuscript version of the following contribution:

Marino, A., Anitra, A., Mazzola, S. M., Di Salvo, T., Sanna, A., Bult, P., Guillot, S., Mancuso, G., Ng, M., Riggio, A., et al. (2022). ***Outflows and spectral evolution in the eclipsing AMXP SWIFT J1749.4–2807 with NICER, XMM-Newton, and NuSTAR. Monthly Notices of the Royal Astronomical Society, 515*****(3), 3838–3852.***

The publisher's version is available at:
https://doi.org/10.1093/mnras/stac2038

When citing, please refer to the published version.

This full text was downloaded from UNICA IRIS https://iris.unica.it/

Outflows and spectral evolution in the eclipsing AMXP SWIFT J1749.4–2807 with *NICER*, *XMM-Newton*, and *NuSTAR*

A. Marino [1,2,3,4★] A. Anitra,[3] S. M. Mazzola,[5] T. Di Salvo [3] A. Sanna [5] P. Bult,[6,7] S. Guillot [8,9] G. Mancuso [10,11] M. Ng,[12] A. Riggio,[5,4] A. C. Albayati [13] D. Altamirano,[13] Z. Arzoumanian,[7] L. Burderi,[5] C. Cabras,[5] D. Chakrabarty,[12] N. Deiosso [5] K. C. Gendreau,[7] R. Iaria [3] A. Manca[5] and T. E. Strohmayer[7,14]

[1]*Institute of Space Sciences (ICE, CSIC), Campus UAB, Carrer de Can Magrans s/n, E-08193 Barcelona, Spain*
[2]*Institut d'Estudis Espacials de Catalunya (IEEC), Carrer Gran Capità 2–4, E-08034 Barcelona, Spain*
[3]*Università degli Studi di Palermo, Dipartimento di Fisica e Chimica, via Archirafi 36, I-90123 Palermo, Italy*
[4]*INAF/IASF Palermo, via Ugo La Malfa 153, I-90146 Palermo, Italy*
[5]*Università degli Studi di Cagliari, Dipartimento di Fisica, SP Monserrato-Sestu km 0.7, I-09042 Monserrato, Italy*
[6]*Department of Astronomy, University of Maryland, College Park, MD 20742, USA*
[7]*Astrophysics Science Division, NASA Goddard Space Flight Center, Greenbelt, MD 20771, USA*
[8]*CNRS, IRAP, 9 avenue du Colonel Roche, BP 44346, F-31028 Toulouse Cedex 4, France*
[9]*Université de Toulouse, CNES, UPS-OMP, F-31028 Toulouse, France*
[10]*Instituto Argentino de Radioastronomía (CCT-La Plata, CONICET; CICPBA), C.C. No. 5, 1894 Villa Elisa, Argentina*
[11]*Facultad de Ciencias Astronómicas y Geofísicas, Universidad Nacional de La Plata, Paseo del Bosque s/n, 1900 La Plata, Argentina*
[12]*MIT Kavli Institute for Astrophysics and Space Research, Massachusetts Institute of Technology, Cambridge, MA 02139, USA*
[13]*School of Physics and Astronomy, University of Southampton, Southampton SO17 1BJ, UK*
[14]*Joint Space-Science Institute, NASA's Goddard Space Flight Center, Greenbelt, MD 20771, USA*

Accepted 2022 July 18. Received 2022 July 16; in original form 2022 April 4

ABSTRACT

The neutron star low-mass X-ray binary SWIFT J1749.4–2807 is the only known eclipsing accreting millisecond X-ray pulsar. In this manuscript, we perform a spectral characterization of the system throughout its 2021, 2-week-long outburst, analysing 11 *NICER* observations and quasi-simultaneous *XMM-Newton* and *NuSTAR* single observations at the outburst peak. The broad-band spectrum is well-modelled with a blackbody component with a temperature of ∼0.6 keV, most likely consistent with a hotspot on the neutron star surface, and a Comptonization spectrum with power-law index $\Gamma \sim 1.9$, arising from a hot corona at ∼12 keV. No direct emission from the disc was found, possibly due to it being too cool. A high truncation radius for the disc, i.e. at ∼20–30 R_G, was obtained from the analysis of the broadened profile of the Fe line in the reflection component. The significant detection of a blue-shifted Fe XXVI absorption line at ∼7 keV indicates weakly relativistic X-ray disc winds, which are typically absent in the hard state of X-ray binaries. By comparing the low flux observed during the outburst and the one expected in a conservative mass-transfer, we conclude that mass-transfer in the system is highly non-conservative, as also suggested by the wind detection. Finally, using the *NICER* spectra alone, we followed the system while it was fading to quiescence. During the outburst decay, as the spectral shape hardened, the hotspot on the neutron star surface cooled down and shrank, a trend which could be consistent with the pure power-law spectrum observed during quiescence.

Key words: accretion, accretion discs – stars: neutron – X-rays: binaries – X-rays: individuals: Swift J1749.4-2807.

1 INTRODUCTION

Accreting millisecond X-ray pulsars (AMXPs) are low-mass X-ray binaries (XRBs) harbouring X-ray pulsars spinning at frequencies of about hundreds of Hz (see for reviews Patruno & Watts 2021; Campana & Di Salvo 2018; Di Salvo & Sanna 2022). Since the discovery of the first AMXP (SAX J1808.4-3658, Wijnands & van der Klis 1998), millisecond X-ray pulsations have been found in 24 other systems, the most recent ones being MAXI J1816-195 (Bult et al. 2022) and MAXI J1957 + 032 (Ng et al. 2022). All AMXPs are transients and a large number of them have been seen only once in outburst and for relatively short periods. However, a few systems stand out for having been observed quite often in outburst (e.g. SAX J1808.4-3658, which in 2019 went in outburst for the eighth time, Bult et al. 2020) or over time-scales of years (e.g. HETE J1900.1-2455 or MAXI J0911-655, Patruno 2012; Sanna et al. 2017b). Almost all AMXPs have short, i.e. ∼hours or minutes, orbital

periods and are therefore characterized by compact orbits, which can accommodate only very low-mass companion stars, typically below 0.5 $M_\odot$. From a spectral point of view, the emission from these systems in outburst is usually dominated by the Comptonization spectrum from a hot corona with electron temperatures kT_e usually of tens of keV (Di Salvo & Sanna 2022). The disc and the neutron star/boundary layer spectra are usually found with relatively low temperatures, i.e. below 1 keV. According to the canonical subdivision in hard and soft spectral states in XRBs (see e.g. Done, Gierliński & Kubota 2007, for a review), AMXPs in outburst are therefore (almost) always in hard state, with SAX J1748.9-2021 (Pintore et al. 2016) and SAX J1808.4-3658 (Di Salvo et al. 2019) as perhaps the only sources observed to transition into the soft state. An additional spectral component arises from the Comptonization spectrum emitted by the corona, which hits the disc and it is thereby reprocessed by it; this component is a dubbed reflection spectrum, and it is a very common ingredient in XRBs spectra (Fabian et al. 1989).

Reflection components are characterized by a forest of emission lines, the most remarkable one being the iron K line at 6.4–6.7 keV, and an excess at 10–30 keV called Compton hump. A proper investigation of these spectral features provides the opportunity to get insights on, e.g. the inner radius of the accretion disc, the ionization of the plasma in the disc, and the inclination of the system. Reflection features have been found in most AMXPs (but not all, see e.g. Miller et al. 2003; Falanga et al. 2005; Sanna et al. 2018a,b), for which data with high-to-moderate energy resolution were available (see e.g. Papitto et al. 2010, 2013; Sanna et al. 2017a). Interestingly, the presence of disc winds, a common ingredient in X-ray spectra of high inclination XRBs during their soft state (Ponti et al. 2012), has been established for one AMXP, i.e. IGR J17591–2342 (Nowak et al. 2019), while tentative detections have been obtained also for SAX J1808.4-3658 (Di Salvo et al. 2019) and IGR J17062–6143 (e.g. van den Eijnden et al. 2018). Finally, most of these systems are bursters, as they have at least once displayed a type-I X-ray burst.

All of these characteristics make AMXPs remarkably similar to another class of XRBs, the Very Faint X-ray Transients (VFXTs; Muno et al. 2005; King & Wijnands 2006; Wijnands et al. 2006). These sources are known to exhibit fainter outbursts with respect to the typical ranges observed in XRBs, with peak luminosity at about 10^{36} erg s^{-1} and even lower (e.g. Del Santo et al. 2007; in't Zand et al. 2009; Degenaar et al. 2017). The origin of such peculiar behaviour is not established yet (for a discussion on the proposed explanation, see e.g. the introduction of Bahramian et al. 2021), because of the relatively scarce data from these objects. In a specific subclass of the VFXTs family, the burst-only systems, the source is only detected during the type-I X-ray burst, as its persistent emission stays below the detection threshold of the All-Sky Monitors active at the time of the observation (Cocchi et al. 2001; Cornelisse et al. 2002; Campana 2009). Even if AMXPs are usually not as faint as VFXTs, the latter ones sometimes display brighter outbursts, i.e. at 10^{36}–10^{37} erg s^{-1} (the 'hybrid' VFXTs, Del Santo et al. 2010; Marino et al. 2019a). Furthermore, a number of systems have been already identified as both AMXPs and VFXTs. An example can be found among the so-called transitional millisecond pulsars or tMSPs (see for a recent review, Papitto & de Martino 2022). This small group consists of three binary millisecond pulsars that switch between a rotation-powered state, where they appear as radio pulsars, and an accretion-powered state (Archibald et al. 2009, 2013; de Martino et al. 2013; Bassa et al. 2014; Papitto et al. 2015, 2019). The typical X-ray luminosity shown by tMSPs in their 'disc state', i.e. about 10^{34} erg s^{-1} or lower, is comparable to the ones shown by VFXTs, and it has been indeed proposed that all VFXTs may be tMSPs in active state (Heinke et al. 2015). Despite being usually found in such a subluminous state, in at least one tMSP, a brighter, AMXP-like, outburst has been observed (Papitto et al. 2015), somehow bridging the gap between tMSPs and AMXP. Finally, three systems who displayed VFXT activity in the past have been later identified also as AMXPs: IGR J17494-3030 (Ng et al. 2021), MAXI J1957 + 032 (Ng et al. 2022), and Swift J1749.4–2807 (see below).

1.1 Swift J1749.4–2807

SWIFT J1749.4–2807 was discovered in 2006 during a type-I X-ray burst (Wijnands et al. 2009) and initially mistaken for a γ-ray burst (Schady et al. 2006). The following X-ray activity of the source was very peculiar as the system reached the peak at a luminosity of about 5×10^{35}erg s^{-1} (for a 7 kpc distance) and faded to quiescence within a day (Wijnands et al. 2009; Campana 2009). The behaviour is consistent with the system being a burst-only source. By assuming that the observed burst reached the Eddington limit for a typical neutron star (NS) mass, an upper limit on the distance of 6.7 ± 1.3 kpc was posed. SWIFT J1749.4–2807 was observed again by the International Gamma-Ray Astrophysics Laboratory (*INTEGRAL*; Winkler et al. 2003) in 2010, during its monitoring campaign of the Galactic Centre (Pavan et al. 2010; Ferrigno et al. 2011). *Swift* and Rossi X-ray Timing Explorer (*RXTE*; Bradt, Rothschild & Swank 1993) Target of Opportunity (ToO) observations were promptly triggered and X-ray pulsations at 518 Hz were discovered (Altamirano et al. 2011), allowing SWIFT J1749.4–2807 to be classified as an AMXP. The orbital ephemeris were determined by Belloni (2010) and Strohmayer & Markwardt (2010), who found that the system has an orbital period of 8.82 h. The *RXTE* light curve also showed X-ray eclipses (Markwardt & Strohmayer 2010), making SWIFT J1749.4–2807 the first, and so far only, eclipsing AMXP. The inclination of the binary is therefore well-constrained in the range 76–77° (Altamirano et al. 2011). Contrarily to the other AMXPs, for which the mass of the donor is usually unknown, the precise determination of the inclination also enabled the companion star mass to be constrained, i.e. in the range ∼0.5–0.8 $M_\odot$ (for an NS mass comprised between 1.0 and 2.2 $M_\odot$). In quiescence, the cooling of the NS was followed in X-rays by Degenaar, Patruno & Wijnands (2012) and an attempt of finding its NIR/optical counterpart was performed by D'Avanzo et al. (2011). On 2021 March 1, after almost 11 yr, JEM-X onboard *INTEGRAL* caught SWIFT J1749.4–2807 in a bright outburst again (Mereminskiy et al. 2021). Coherent pulsations were also detected in this case, this time with *NICER* (Bult et al. 2021b).

In this manuscript, we present a detailed broad-band X-ray spectral analysis of this peculiar object during its latest outburst. In the first part of this work, we analyse the 0.8–50 keV broad-band spectrum of the system using *XMM-Newton*, *NuSTAR*, and *NICER* data (Section 3.1), while in the second one we individually analyse 11 *NICER* observations covering the short-lived outburst, from rise to decay (Section 3.3). The main results obtained in this work are discussed in Section 4, while summary and conclusions are presented in Section 5.

2 OBSERVATIONS AND DATA REDUCTION

The 2021 outburst of SWIFT J1749.4–2807 was the object of a number of pointed observations from different X-ray telescopes. In this paper, we exploit the data collected by *XMM-Newton*, *NICER*, and *NuSTAR*. A summary of the observations is reported in Table 1. More details on the data reduction for each instruments are given in the following sections.

Table 1. List of the *XMM-Newton* , *NuSTAR*, and *NICER* observations of the source used in this work. With †, we indicated the *NICER* observation quasi-simultaneous, i.e. taken within the same day, to *XMM-Newton* and *NuSTAR* used in the broad-band spectral analysis (Section 3.1).

	ObsID	Start time (UTC)	(MJD)	Exposure ks
		XMM-Newton		
	0872392001	2021-03-04	59277.01	57.9
		NuSTAR		
	90701310002	2021-03-04	59277.30	49.4
		NICER		
N01	4658010101	2021-03-01	59274.62	9.3
N02	4658010102	2021-03-02	59275.00	18.2
N03	4658010103	2021-03-03	59276.03	9.8
N04	4658010104†	2021-03-04	59277.01	11.6
N05	4658010105	2021-03-05	59278.04	17.0
N06	4658010106	2021-03-08	59281.20	5.3
N07	4658010107	2021-03-09	59282.04	11.3
N08	4658010108	2021-03-10	59283.01	12.0
N09	4658010109	2021-03-11	59284.11	8.6
N10	4658010110	2021-03-12	59285.01	7.4
N11	4658010111	2021-03-13	59286.17	4.5

2.1 XMM-Newton

The *XMM-Newton* observation was performed on 2021 March 4 between 01:10:36 UTC and 02:26:17 UTC for a duration time of 57.9 ks. The two MOS detectors of the European Photon Imaging Camera (EMOS; Turner et al. 2001) were operating in Imaging and Timing mode, respectively, while the PN-type charge-coupled device (CCD) detector (Epic-PN, hereafter EPN; Strüder et al. 2001) was in Timing mode. The Reflecting Grating Spectrometer (two modules, den Herder et al. 2001) was functioning in standard spectroscopy mode. We reprocessed the data using the *XMM-Newton* Science Analysis Software (SAS) v18.0.0. We produced calibrated photon event files using reprocessing tools `emproc`, `epproc`, and `rgsproc` for EMOS, EPN, and RGS data, respectively. We verified the absence of flare events in the EPN data, extracting the light curve in the 10–12 keV energy range, and we checked out the presence of pile-up contamination for MOS1: we used the task `epatplot` that, displaying the observed pattern distribution versus the expected one, allowed us to show how the pile-up fraction was not negligible. Therefore, we decided to use only EPN and MOS2 data for the analysis, as the count-rates of the collected data (40 counts/s and 19 counts/s) were below the pile-up threshold reported for the detectors (800 counts/s and 100 counts/s for EPN and MOS operating in timing mode, respectively). We extracted the EPN 0.2–15 keV light curve considering PATTERN ≤ 4, to extract only single and double good events, and FLAG $= 0$ from a rectangular region, which included the brightest columns of the detector (between RAWX ≥ 30 and RAWX ≤ 45). For the background, we extracted the events from a region far away from the source, between RAWX ≥ 5 and RAWX ≤ 20. Meanwhile, for MOS2 data, we selected the columns in the interval 289$\leq$RAWX$\leq$327 for the source and we extracted background from a region of the outer CCDs, which were functioning in imaging mode, as suggested by SAS Data Analysis Threads.[1] To verify the presence of dips or eclipses, we extracted the 0.2–3 and 3–10 keV EPN light curve and calculated the hardness ratio. (HR) We observed two complete eclipses between 1.05 and 3.42 ks, and between 32.80 and 35.10 ks from the start time, and a partial eclipse at the end of the observation (starting at 46.80 ks). With the same aim, we accumulated the MOS2 light curve with a bin time of 100 s, considering PATTERN$\leq$0 and FLAG $= 0$, observing one eclipse between 29.96 and 32.22 ks from the start time. Furthermore, six Type-I X-ray bursts were detected by both cameras during the observation.

Finally, we used `tabgtigen` task to create the good time interval (GTI) file for both bursts and eclipses, and the `xmmselect` task to extract the 0.2–15 keV light curve and spectrum of the persistent emission, excluding the time intervals at which the bursts and the eclipses occurred, which will be investigated elsewhere (Mancuso et al., in preparation). Also, the RGS light curve of this observation (produced combining RGS1 and RGS2 light curves with `rgslccorr`) showed bursts and eclipses, as observed in EPN data. Then, we used the same procedure to filter them and obtained the persistent spectrum running the task `rgsproc` until the '`fluxing`' final stage. Then we combined the first-order spectra of RGS1 and RGS2 through `rgscombine` to obtain the total RGS spectrum and the related response matrix (rmf) and ancillary file (arf).

2.2 NuSTAR

NuSTAR observed the system on 2021 March 4, for a total exposure of 49.4 ks. We reduced the data using the standard `Nustardas` task, incorporated in HEASOFT (v. 6.26.1) and using the latest CALDB version available. The source was selected by means of a circular area of 100 arcsec radius, centred at the coordinates of the source, i.e. R.A. (J2000) $= 17^{h}49^{m}31.940^{s}$, Dec. (J2000) $= -28^{\circ}08'05.89''$ (Roming et al. 2009). In order to take into account any background non-uniformity on the detector, we extracted the background spectra using four circles of $\sim$50 arcsec radii placed on different areas of the image characterized by having negligible contamination from the source. We then used `Nuproducts` to build spectra and light curves. Also, in this case, eclipses and bursts (if present) were excluded when creating the final products. We used data from both the hard X-ray imaging telescopes on board *NuSTAR*, i.e. the focal plane mirrors (FPM) A and B. Finally, we did not sum the FPMA and FPMB spectra, but rather fitted them simultaneously by leaving a floating cross-normalization constant.[2]

2.3 NICER

NICER monitored the 2021 outburst of SWIFT J1749.4–2807 with almost daily cadence (see Table 1). In this work, we analysed the whole sample of these *NICER* observations. Data were reduced using `nicerl2` task (`NICERDAS 2019-05-21 v006`): we set recommended calibration processes, standard screening and we added the `niprefilter2_coltypes = base,3c50` parameter so that the `3C 50` model can be used to derive background spectra later. We extracted the cleaned event files, checking that all detectors were active during observations and excluding data from two of them (labelled 14 and 34), in order to reduce the detector noise. We accumulated light curves from all the observations using the `xselect` tool, finding several eclipses and bursts that we excluded from our analysis. Then we selected the GTI using

[1] https://www.cosmos.esa.int/web/xmm-newton/sas-thread-mos-spectrum-timing

[2] In accordance with the guidelines from the *NuSTAR* team, see FAQ page, issue 19: https://heasarc.gsfc.nasa.gov/docs/nustar/nustar_faq.html

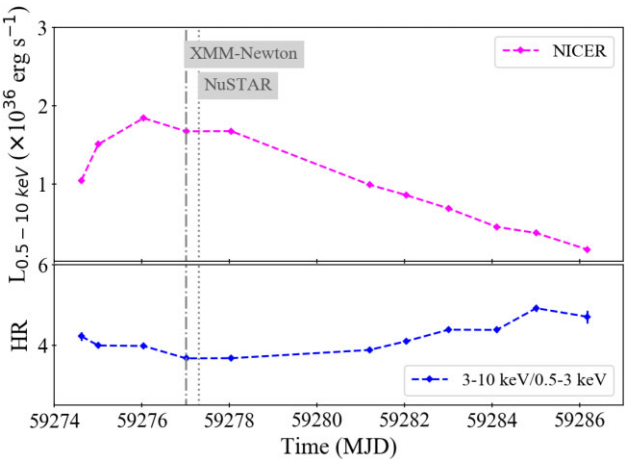

Figure 1. (*Top*) *NICER* light curve of SWIFT J1749.4–2807 in X-ray (0.5–10 keV) luminosity (calculated for a 6.7 kpc distance) and relative HR (*bottom*). The times of the *XMM-Newton* and *NuSTAR* observations are highlighted with dash–dotted and dotted grey lines, respectively. The hardness values have been obtained by measuring the ratio between fluxes in the hard (3–10 keV) and soft (0.5–3 keV) bands, as estimated from the spectral analysis.

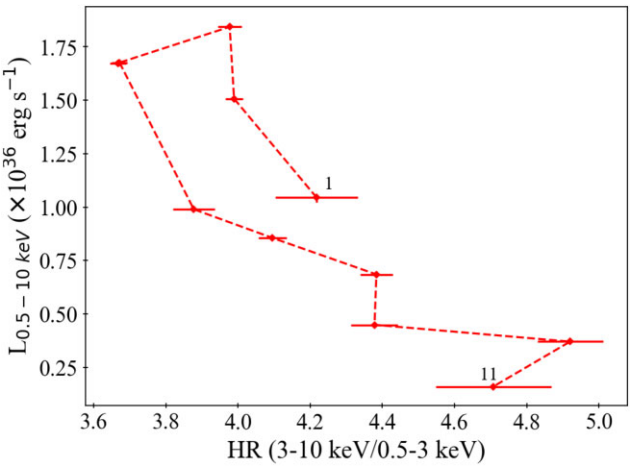

Figure 2. *NICER* HID. The positions of the first and the last (11th) epochs are reported for clarity. The hardness values have been obtained by measuring the ratio between fluxes in the hard (3–10 keV) and soft (0.5–3 keV) bands, as estimated from the spectral analysis.

`NIMAKETIME` and applied them to the data via `NIEXTRACT-EVENTS`, selecting events with PI channel between 25 and 1200 (0.25–12.0 keV).We used the `nibackgen3C50` tool to extract both the spectra of the source and the background from the cleaned event files, selecting the 2020 gain calibration. Finally, we exploited the public files `nixtiaveonaxis20170601v002.arf` and `nixtiref20170601v001.rmf` as Ancillary Response File and Redistribution Matrix File, respectively, retrievable from the *NICER* website.[3]

3 SPECTRAL ANALYSIS

The *NICER* light curve of the system is shown in Fig. 1. The *XMM-Newton* and *NuSTAR* observations (highlighted in Fig. 1 with vertical grey lines) have been taken the same day, around the peak of the outburst. In order to follow the spectral evolution of the system throughout the outburst, we analysed each of the *NICER* spectra with XSPEC (see Section 3.3 for more details on the spectral fitting procedure) and extracted by means of `cflux` the X-ray flux in three bands: 0.5–10 keV, 0.5–3 keV (soft band), 3–10 keV (hard band). We then plotted the 0.5–10 keV flux versus the HR to produce the Hardness Intensity Diagram (HID), shown here in Fig. 2. As apparent from the HID, the source remained quite spectrally stable throughout the whole outburst, with the hardness ranging only from 3.5 at the outburst peak to 5 at its culmination.

In the following sections, we proceed first (Section 3.1) by analysing a broad-band spectrum, including the *XMM-Newton* and *NuSTAR* data, and the *NICER* observation that was the closest in time with those pointings, i.e. ObsID 4658010104. In the *NuSTAR* spectrum, we ignored data below 4 keV because of a mismatch between FPMA and FPMB, likely due to a known instrumental issue (Madsen et al. 2020). *NuSTAR* data higher than 50 keV were ignored as well, as they appear background dominated. Similarly, RGS and *NICER* data below 1 and 0.8 keV, respectively, were submerged by the instrument background and therefore neglected. EPIC-PN showed an excess below 1.5 keV, which was not present in *NICER* and EPIC-MOS 2 data instead. Reports of similar excesses have been noticed several times in observations of bright objects performed by Epic-PN data in timing mode (see e.g. D'Aì et al. 2010; Egron et al. 2013, and references therein) and sometimes ascribed to calibration issues. We therefore kept EPIC-PN data only between 2.4 and 10 keV, in order to ignore the 1.8 keV (Si K-edge) and 2.3 keV (Au M-edge) instrumental features as well. All the data used in this work were grouped exploiting the optimal binning recipe by Kaastra & Bleeker (2016), which allows to have a grouping, reflecting the spectral resolution of the instrument in a given energy range and prevents any oversampling issue.

We then exploit the whole set of *NICER* observations to perform a round of analyses on each *NICER* spectrum, hunting for possible evolution of the physical parameters of the system throughout the whole outburst. The results of such finer analysis are presented in Section 3.3.

We used XSPEC v12.10.1f to perform the spectral fit. For each analysed observation, we included the TBABS component in the spectral model to take into account the effect of the interstellar absorption, setting the photoelectric cross-sections and the element abundances to the values provided by Verner et al. (1996) and Wilms, Allen & McCray (2000), respectively. A CONSTANT component was also used to serve as cross-calibration constant.

3.1 Broad-band spectral analysis

3.1.1 Continuum analysis

In order to probe the spectral shape of the source, we started by fitting the broad-band *XMM-Newton* - *NICER* - *NuSTAR* spectrum with an absorbed POWERLAW model. The fit residuals reveal the presence of several structures, including a thermal component at low energies, i.e. below 2 keV, and the clear signature of a reflection Compton hump beyond ∼10 keV. We found that the thermal component could be satisfactorily described by a blackbody component from the NS/boundary layer (BBODYRAD), a multicolour disc blackbody (DISKBB or DISKPN; e.g. Gierliński et al. 1999) or a combination of the two models, but selected BBODYRAD only as it gave the most physically reliable fit. Indeed, using only BBODYRAD, we obtain a

[3] See https://heasarc.gsfc.nasa.gov/docs/nicer/proposals/nicer_tools.html.

blackbody temperature $kT_{\rm bb}$ of ∼0.7 keV and a radius $R_{\rm bb}$[4] of about ∼5 km, compatible with the presence of a hotspot on the NS surface. On the contrary, including only one disc component, as DISKBB or alternatively a more sophisticated model such as DISKPN, leads inevitably to unphysical results. A DISKBB at a temperature of about 1 keV could, in principle, replace BBODYRAD, but the relatively small normalization $K_{\rm disc}$ value obtained would translate[5] into a rather small inner radius of the disc, i.e. of ∼2 km, which is non-physical for an accreting NS. Similarly, a single DISKPN component, at a temperature of ∼1.0 keV and an inner radius of 50 $R_{\rm G}$, provides an acceptable fit, but in order to explain the very low value found for the normalization $K_{\rm diskpn}$ we need to invoke a distance D of about 60 kpc,[6] almost 10 times higher than the distance range estimated for the system (Wijnands et al. 2009). Keeping both BBODYRAD and DISKBB returns a statistically acceptable fit as well, but the normalization $K_{\rm disc}$ attained extremely high ($>2 \times 10^4$) values this time, which would require inner radii higher than 400 km, which is rather odd (for the truncation radii typically found in this class of system, see e.g. van den Eijnden et al. 2017, and references therein). Using DISKPN instead of DISKBB does not solve the issue, as the distance D required to justify the obtained normalization value would be lower than 1 kpc.

In order to reproduce correctly both Comptonization and reflection spectra, we replaced the POWERLAW with RELXILLCP (García et al. 2014). The main parameters of the model are therefore: the BBODYRAD temperature $kT_{\rm bb}$ and normalization $K_{\rm bb}$, the disc emissivity ϵ, the inclination of the system i, the inner radius of the disc $R_{\rm in}$, the electron temperature of the corona $kT_{\rm e}$, the ionization ξ, the iron abundance $A_{\rm Fe}$, and the reflection fraction $f_{\rm refl}$. The inclination of the system is known from the study of the eclipses, so that it was fixed to the value 76.9° (Altamirano et al. 2011). In all the performed fits, we also froze ϵ to 3 (a value commonly found in XRBs, see e.g. Dauser et al. 2013; Marino et al. 2019a) and $A_{\rm Fe}$ to 1.0, since the fit was unable to find constraints on them. Finally, in order to account for small differences in calibration, we did not tie the power-law photon index Γ between the *NICER* and EPN and MOS 2 spectra. We checked systematically that discrepancies between the best-fitting values obtained for Γ were always lower than 10 per cent. We notice that the seed photon temperature of the Comptonization can not be changed and it is set to be very low, i.e. $kT_{\rm seed} \lesssim 0.1$ keV, i.e. compatible with a cold, possibly truncated, disc.

The overall shape of the spectrum was well-fitted with this model: χ^2_ν(d.o.f.) = 1.38(670). According to this analysis, the photon index Γ of the spectrum was about 1.9, the NS surface was emitting at a blackbody temperature of ∼0.7 keV, the blackbody radius was found to be ∼5 km, the corona had an electron temperature of 12–14 keV, the disc was truncated at a radius of about 20–34 $R_{\rm G}$ and the fraction of reflected photons was around 0.1.

[4]In BBODYRAD, the normalization parameter $K_{\rm bb}$ found by the spectral fit is connected to the blackbody radius $R_{\rm bb}$ by the formula $K_{\rm bb} = (R_{\rm bb}/D_{10\,\rm kpc})^2$, with $D_{10\,\rm kpc}$ the distance of the source in units of 10 kpc.

[5]We converted the normalization into the inner disc radius by taking advantage of the relation: $K_{\rm diskbb} = (R_{\rm in}/D_{10})^2 \cos i$, with $K_{\rm diskbb}$ the DISKBB normalization and D_{10} the distance of the system in 10 kpc units, and using the colour correction factors $\kappa = 1.7$ and a ξ correction factor for the torque-free boundary condition of 0.42 (Kubota et al. 1998; Gierliński & Done 2002).

[6]Since, $K_{\rm diskpn}$ can be expressed as $K_{\rm diskpn} = M_{\rm NS} \cos i/(D^2 f^4)$, with f the ratio between colour and effective disc temperatures, we calculated the distance by assuming typical values for $M_{\rm NS}$(1.5 $M_\odot$), f (1.7), the known inclination of the system (77°) and the value of $K_{\rm diskpn}$ obtained by the fit.

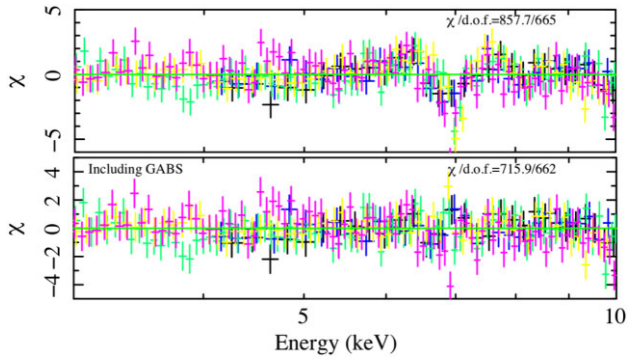

Figure 3. Comparison between the residuals obtained with different models in the range 3–10 keV. Models tested: `tbabs×(bbodyrad + relxillCp)`, *top panel*; `tbabs×gabs×(bbodyrad + relxillCp)`, *bottom panel*. Data: *NICER* (green), *XMM-Newton*/EPIC-pn (yellow), EPIC-MOS2 (magenta), and *NuSTAR* (blue–black).

3.1.2 Analysis of the absorption feature

Despite the acceptable fit, some local residuals still existed, as shown in Fig. 3. In particular, the presence of a pronounced dip around 7 keV clearly pointed out the presence of an absorption feature. In order to fit it, we initially included the multiplicative GABS component. The obtained value of $E_{\rm line}$ indicates that the feature is a slightly blueshifted absorption line from Fe XXVI, as commonly found for high inclination LMXBs (see e.g. Ponti, Muñoz-Darias & Fender 2014). As the detection of such a feature indicates the presence of ionized absorbing plasma in the system, we also included ZXIPCF, which takes into account the case where a fraction $f_{\rm abs}$ of the source is covered by absorbing photoionized matter, with ionization parameter $\xi_{\rm abs}$. The model was initially developed for active galactic nuclei (Miller 2007; Reeves et al. 2008), but it has been applied to high inclination XRBs as well (see e.g. Ponti et al. 2015; Iaria et al. 2020). Besides of $f_{\rm IA}$ and $\xi_{\rm IA}$, the main parameter of the model is the equivalent hydrogen column of the material, $N_{\rm H,\,IA}$. The ZXIPCF component is in principle able to reproduce also the Fe XXVI line. However, in our case, keeping GABS in the model was necessary to fully clear the residuals (see e.g. Ponti et al. 2015, for a discussion). We also attempted to replace GABS with a second ZXIPCF component but, in spite of a clear improvement in the residuals and in the fit, the parameters in the second ZXIPCF were left completely unconstrained by the fit. We therefore decided to use only one ZXIPCF component and GABS for the spectral analysis.

According to our results, the absorbing material described by ZXIPCF covers a fraction of 10 per cent or lower of the X-ray main source and it is characterized by a high ionization ($\log \xi_{\rm IA}$ between 3 and 4.5) and high $N_{\rm H,\,IA}$ (lower limit of $\sim 3 \times 10^{24}$ cm^{-2}). The Fe XXVI line was successfully fitted with GABS at an energy $E_{\rm line}$ of $6.99^{+0.03}_{-0.02}$ keV, an associated optical depth at the centre of about $\tau_{\rm line}$ ∼ 0.2, and an equivalent width of∼40 eV. Such a feature is found to be significantly blueshifted with respect to its rest-frame energy, i.e. 6.9662 keV (Verner et al. 1996), indicating an outflowing disc wind at a velocity $v_{\rm out}$ of ∼600–2700 km s^{-1}. In order to further investigate the line profile, we applied the Goodman–Weare algorithm of Monte Carlo Markov Chain (MCMC; Goodman & Weare 2010) to produce contour plots for $E_{\rm line}$ and $\tau_{\rm line}$. We used 20 walkers and a chain length of 5×10^5 to calculate the marginal posterior distributions of the best-fitting parameters. The same procedure was applied to the spectra of *NICER* , *NuSTAR* (including both FPMA and FPMB), Epic-PN, and Epic-MOS 2 taken singularly, with the aim to explore how the

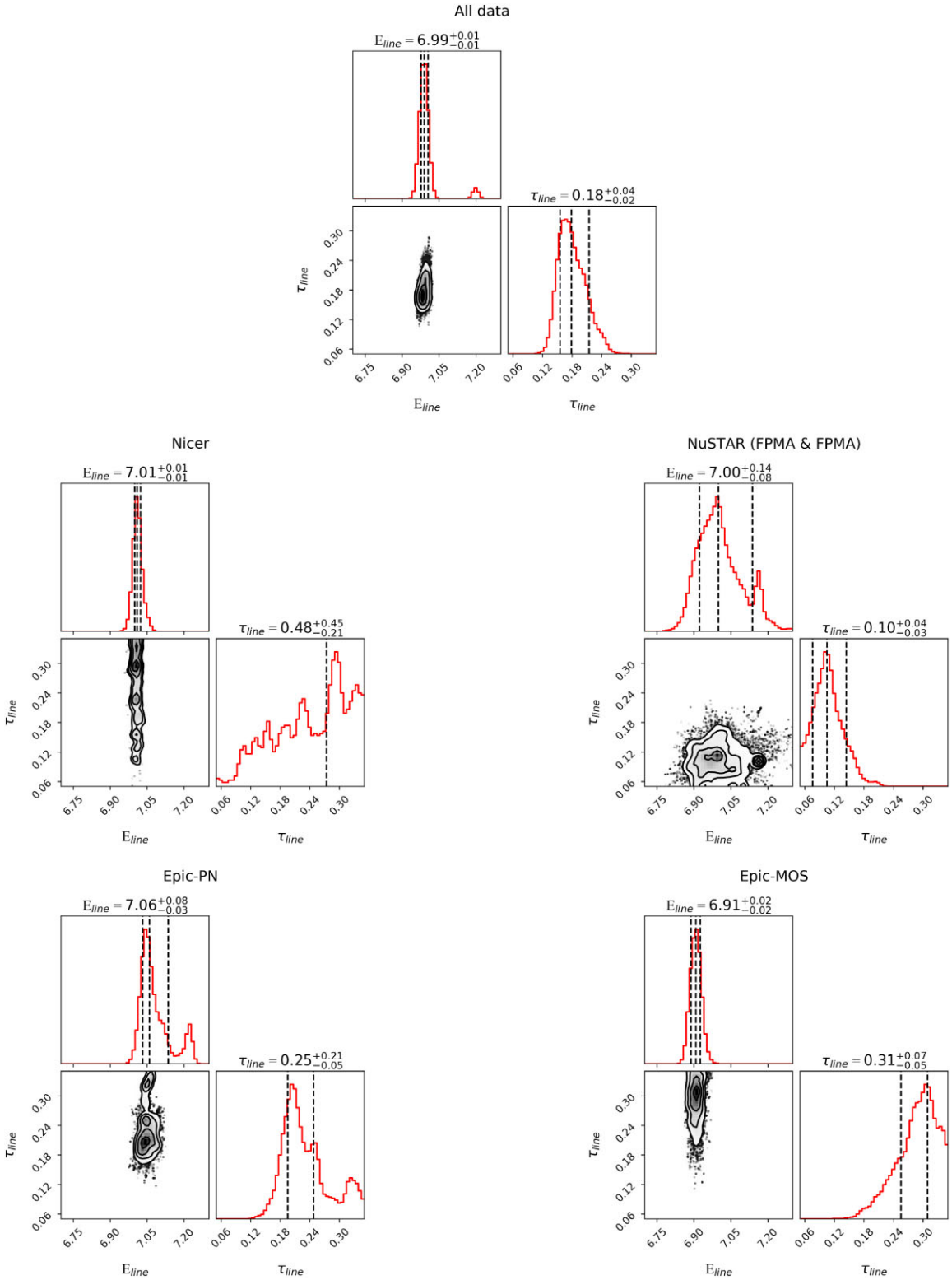

Figure 4. Posterior probability distributions for $E_{\rm line}$ and $\tau_{\rm line}$ for the entire data set (top panel), *NICER* (middle left), *NuSTAR* (middle right), Epic-PN (bottom left), and Epic-MOS 2 (bottom right). Contours represent the 1σ, 2σ, and 3σ confidence levels. Marginal posterior distributions are shown as histograms with the median and 1σ intervals of confidence highlighted as dashed lines.

feature is observed by the different instrument. As apparent, some level of discrepancy between the line profile seen by the different instruments has to be taken into account, especially with regards to Epic–MOS 2. Such a discrepancy could be a symptom of a residual level of pile-up or some other systematics in MOS 2. The results are presented in Fig. 4, where the MCMC chains are visualized by means of `corner.py` (Foreman-Mackey 2016). Finally, a second feature could be appreciated in emission around 1.7 keV in the

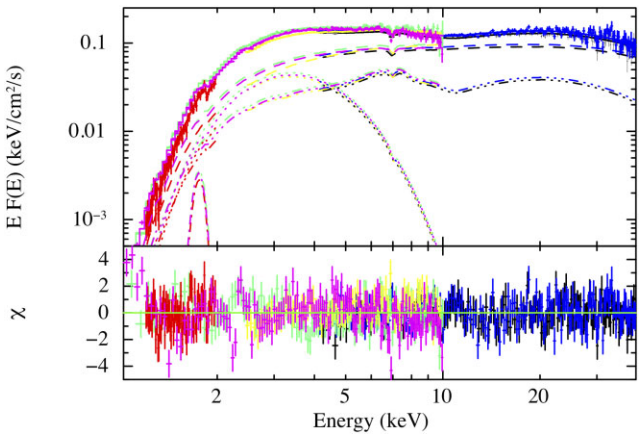

Figure 5. Energy spectra, best-fitting model, and residuals for Epoch 4. Data: *NICER* (green), *XMM-Newton*/EPIC-pn (yellow), EPIC-MOS2 (magenta), *XMM-Newton*/RGS (red), and *NuSTAR* (blue–black). Different line styles were adopted to distinguish between the different components: dot for BBODYRAD, dash for RELXILLCP, and dash-dot-dot-dot for RELXILLCP with the parameter $f_{\rm refl}$ set negative in order to highlight the pure reflection component, and dash-dot for the instrumental GAUSSIAN at 1.7 keV, due to Si fluorescence.

Table 2. Fit results. Quoted errors reflect 90 per cent confidence level. The parameters that were kept frozen during the fits are reported between round parentheses.

Broad-band **spectral analysis** *NICER* + *XMM-Newton* + *NuSTAR*			
model: tbabs×zxipcf×gabs×(relxillCp + bbodyrad)			
Model	**Parameter**		
TBABS	$N_{\rm H}$	(10^{22} cm^{-2})	4.62 ± 0.05
ZXIPCF	$N_{\rm H,\,abs}$	(10^{22}cm^{-2})	>280
	$\log \xi_{\rm abs}$		$4.0^{+0.6}_{-1.1}$
	$f_{\rm cov}$		0.07 ± 0.04
BBODYRAD	$kT_{\rm body}$	(keV)	$0.695^{+0.013}_{-0.014}$
	$R_{\rm bb}$	(km)	$5.0^{+1.5}_{-1.5}$
RELXILLCP	ϵ		(3.0)
	i	(°)	(76.9)
	$R_{\rm in}$	$R_{\rm G}$	26^{+8}_{-6}
	Γ		1.91 ± 0.02
	$kT_{\rm e}$	(keV)	$12.9^{+1.6}_{-1.1}$
	$\log(\xi)$		$3.30^{+0.15}_{-0.13}$
	$A_{\rm Fe}$		(1.0)
	$f_{\rm refl}$		$0.16^{+0.10}_{-0.04}$
	$K_{\rm RELX}$	($\times\ 10^{-4}$)	$9.7^{+1.3}_{-2.2}$
GABS	$E_{\rm line}$	(keV)	$6.99^{+0.03}_{-0.02}$
	$\sigma_{\rm line}$	(keV)	0.11 ± 0.06
	$\tau_{\rm line}$		0.17 ± 0.02
	χ^2_ν	(d.o.f.)	**1.07(660)**

NICER residuals. Then, we added a second GAUSSIAN line (this time with positive normalization) and found it significant (5.5σ) at an $E_{\rm line,\,2}$ of 1.71 keV and a $\sigma_{\rm line,\,2}$ of ∼0.01 keV. This narrow feature is most likely a Si fluorescence line from the Focal Plane Modules (M. Corcoran, private communication). The final fit is shown in Fig. 5, while the best-fitting parameters are listed in detail in Table 2.

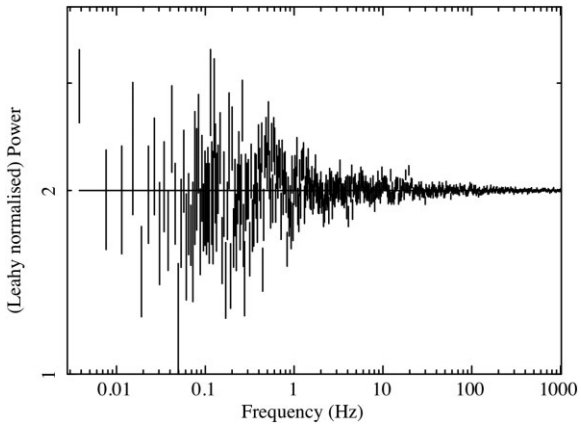

Figure 6. *NICER* power density spectrum for Epoch 4. A CONS model at value 2.0 is displayed as an horizontal black line.

3.2 *NICER* timing analysis

In order to corroborate the spectral state identification, we extracted the Leahy-normalized *NICER* Fourier Power Density Spectrum (PDS) for Epoch 4 in the 0.5–10 keV energy range. We used a bin-time of 5 ms. We did not subtract the Poisson noise contribution, but rather fitted it with a constant component. The obtained PDS and its best-fitting model are shown in Fig. 6. The PDS is consistent with a constant of ∼2 at higher frequencies, compatible with Poisson noise. We obtained a value of about 6 per cent for the overall *rms*. The system shows therefore little to no X-ray variability, in contrast to what typically expected for XRBs in a hard or hard-intermediate state. This will be further discussed in Section 4.

3.3 *NICER* monitoring

In order to follow the evolution of the single physical parameters along the 2-week outburst, we analysed each *NICER* spectrum separately. In the following, we will refer to each of them with labels going from N01 to N11 (see Table 1), in progressive order. We modelled the data in accordance with the results obtained in Section 3.1 with the same continuum model, i.e. TBABS×ZXIPCF×(BBODYRAD + RELXILLCP). However, due to the *NICER* energy range, we kept fixed $kT_{\rm e}$ to 12 keV, in consistency with the results of the broad-band spectral analysis. Furthermore, the reduced energy range with respect to the broad-band spectrum forced us to fix more parameters, as they were left completely unconstrained in the individual fits. This is the case, in particular, for $f_{\rm refl}$, $R_{\rm in}$, $N_{\rm H,\,IA}$, $f_{\rm IA}$, and $\log \xi_{\rm IA}$, kept frozen to the (previously obtained) values of 0.1, 30 $R_{\rm G}$, 500 cm^{-2}, 0.10, and 4.0, respectively. The presence of discrete features around 1.7 keV in emission and around 7 keV in absorption could be easily spotted in the residuals of observations N01–N06, i.e. around the peak of the outburst. In analogy with Section 3.1, they were fitted with a GAUSSIAN and GABS, respectively. However, for the absorption feature, the estimated errors on $E_{\rm line}$ and $\sigma_{\rm line}$ were too large to be meaningful in all spectra, with the exception of observation N04, i.e. the same observation used for the broad-band spectral analysis. We therefore fixed those parameters to 7.0 and 0.10 keV, in analogy with the broad-band spectrum. The best-fitting parameters are reported on Table 3. Despite the large errors, the optical depth $\tau_{\rm line}$ associated with the feature shows an evolution, i.e. going from 0.15 to 0.20 in the observations at the outburst peak (N01–N05) to likely smaller values in the fading part of the outburst, where only upper limits could be posed. In the first six observations, N_H attained values in

Table 3. Results of the spectral analysis of the single *NICER* spectra. Quoted errors reflect 90 per cent confidence level. The parameters that were kept frozen during the fits are reported between round parentheses. [a]: The flux values reported, corresponding to the 0.5–10 keV energy range, have been obtained in the N_H free case.

NICER spectral analysis						
model: tbabs×zxipcf×gabs×(relxillCp + bbodyrad)						
Parameters	N01	N02	N03	N04	N05	N06
$N_{\rm H}$ ($\times 10^{22}$ cm^{-2})	4.30 ± 0.10	4.57 ± 0.07	$4.54^{+0.11}_{-0.10}$	4.65 ± 0.09	4.60 ± 0.08	4.17 ± 0.15
$kT_{\rm bb}$ (keV)	0.596 ± 0.020	$0.645^{+0.013}_{-0.012}$	0.654 ± 0.014	$0.659^{+0.013}_{-0.012}$	0.640 ± 0.013	$0.560^{+0.030}_{-0.040}$
$R_{\rm bb}$ (km)	6.0 ± 2.0	5.5 ± 2.0	6.6 ± 2.0	6.0 ± 2.0	5.6 ± 2.0	5.2 ± 2.5
Γ	$1.54^{+0.09}_{-0.08}$	1.82 ± 0.06	1.76 ± 0.08	1.89 ± 0.07	1.96 ± 0.05	1.77 ± 0.11
$\tau_{\rm line}$	0.11 ± 0.07	0.18 ± 0.05	0.15 ± 0.07	0.18 ± 0.07	0.16 ± 0.05	<0.21
χ^2_ν (d.o.f.)	1.08(106)	0.92(118)	1.03(109)	1.08(115)	1.06(118)	1.01(100)
F_X^a ($\times 10^{-10}$ erg cm^{-2} s^{-1}	$1.944^{+0.050}_{-0.014}$	2.805 ± 0.012	$3.430^{+0.020}_{-0.019}$	3.115 ± 0.013	3.112 ± 0.012	$1.843^{+0.019}_{-0.018}$
	N07	N08	N09	N10	N11	
$N_{\rm H}$ ($\times 10^{22}$ cm^{-2})	$4.05^{+0.11}_{-0.10}$	$4.04^{+0.13}_{-0.12}$	$4.06^{+0.07}_{-0.08}$	3.76 ± 0.08	$2.90^{+0.30}_{-0.20}$	
$kT_{\rm bb}$ (keV)	0.587 ± 0.030	$0.550^{+0.080}_{-0.060}$	(0.500)	(0.500)	$0.580^{+0.090}_{-0.130}$	
$R_{\rm bb}$ (km)	3.8 ± 1.8	$3.0^{+1.9}_{-2.0}$	<2.5	<2.5	$1.7^{+1.8}_{-0.9}$	
Γ	1.76 ± 0.08	1.76 ± 0.08	$1.90^{+0.02}_{-0.07}$	1.68 ± 0.08	< 1.47	
$\tau_{\rm line}$	<0.15	<0.16	<0.21	<0.11	(0.05)	
χ^2_ν (d.o.f.)	1.00(109)	1.12(106)	0.98(98)	1.08(94)	1.05(63)	
F_X^a ($\times 10^{-10}$ erg cm^{-2} s^{-1}	1.594 ± 0.010	1.277 ± 0.009	$0.840^{+0.009}_{-0.008}$	0.691 ± 0.009	$0.300^{+0.008}_{-0.007}$	

the range 4.4–4.6 $\times 10^{22}$ cm^{-2}, while starting with N07, a decreasing trend could be observed in the best-fitting values obtained for $N_{\rm H}$, i.e. going down to $\sim 3 \times 10^{22}$ cm^{-2} in the last observation. Fixing $N_{\rm H}$ to the previously obtained value of $\sim 4.5 \times 10^{22}$ cm^{-2} provided acceptable fits, but with slightly worse χ^2/d.o.f. ratios. In order to check whether such an evolution was significant, we followed the same procedure illustrated in Section 3.1 to calculate the marginal posterior distributions of the best-fitting parameters. The results for four representative observations are presented in Fig. 7. As apparent from the figure, the changes in N_H between different observations are significant, highlighting that N_H should be indeed left free. In the following, we will therefore report only the results obtained for N_H thawed, and discuss the physical implications of that scenario in Section 4. The evolution of the main physical parameters of the system is displayed in Fig. 8.

At the beginning of the outburst, the thermal emission is due to hot spots of about 5–6 km in size and ∼0.6 keV temperature. Towards the peak of the outburst (around observation 5), Γ is characterized by an increasing trend, despite never becoming softer than $\Gamma \sim 2.1$. After the peak, at a 0.5–10 keV X-ray luminosity of only 2×10^{36}erg s^{-1} , the system starts fading to quiescence. During this decay, $kT_{\rm bb}$ decreases slightly (around 0.5 keV) and the hotspot shrinks to about 1–2 km radius. Concerning Γ, a hardening in the power-law index can be observed while the system fades towards quiescence.

4 DISCUSSION

In this manuscript we presented the spectral analysis of SWIFT J1749.4–2807 during its 2021 faint, 2-week lasting outburst. We used data from the *NICER* daily monitoring of this outburst and included *XMM-Newton* and *NuSTAR* data taken at the peak. As in several other AMXPs (see table 2 of Marino et al. 2019b, for an overview of the outburst properties of the class), the system displayed a relatively short and hard outburst, with very little spectral evolution. In the following, we discuss the main findings of this work and their physical implications.

4.1 Geometry of the accretion flow

Both broad-band and individual *NICER* spectra were satisfactorily described with a blackbody component, a thermal Comptonization spectrum and a reflection component. At the peak, the blackbody emission arises from a ∼5–6 km region at a temperature of about 0.6 keV, consistent with a hotspot on the surface of the NS, possibly the magnetic polar caps. The Comptonization spectrum is instead due to 'cold' seed photons (see Section 3.1), according to the assumptions underlying the RELXILLCP model, Compton up-scattered by a 12 keV electron corona into a $\Gamma \sim 1.9$ cut-off power-law. The source of these seed photons is probably attributable to the accretion disc, which is indeed too faint to give a statistically significant contribution to the spectrum or simply too cold for the energy range considered. A small, i.e. $f_{\rm refl}$ ∼10–20 per cent, fraction of these photons are intercepted by the disc and reprocessed, forming the reflection component. Modelling this one with RELXILLCP, we obtained that the disc is truncated quite far from the NS, at a ∼20–34 R_G (44–76 km for a 1.5 $M_\odot$ NS) radius, and it is quite highly ionized, indeed $\log \xi$ is consistent with 3.3. Considering that these estimates should be taken with some caution due to the uncertainties on e.g. the value adopted for the NS mass, the obtained range of values for the inner edge of the disc results roughly compatible with the co-rotation radius $R_{\rm co}$ expected for a NS spinning at 518 Hz, i.e. 31–44 km for a 0.8–2.2 $M_\odot$ NS. It results thereby that the inner edge of the disc and the NS magnetic field lines spin at (almost) the same frequencies and the torque exerted on the NS by the columns of matter funnelled up on to the magnetic field lines should be negligible. According to this result, the NS in SWIFT J1749.4–2807 is expected to be in a spin-equilibrium condition, i.e. not subject to any significant spin-up or spin-down rate. It is noteworthy that the spin derivative obtained in Sanna et al. (2022) are compatible with this scenario. Similar moderate truncation radii have been found in AMXPs that have shown remarkably bright outbursts, such as HETE J1900.1-2455 (Papitto et al. 2013) and SAX J1748.9-2021 (Pintore et al. 2016), but also for the very faint AMXP IGR J17062-6143 (Bult et al. 2021a). If confirmed, this finding would suggest that high truncation radii are not an essential ingredient to obtain subluminous outbursts.

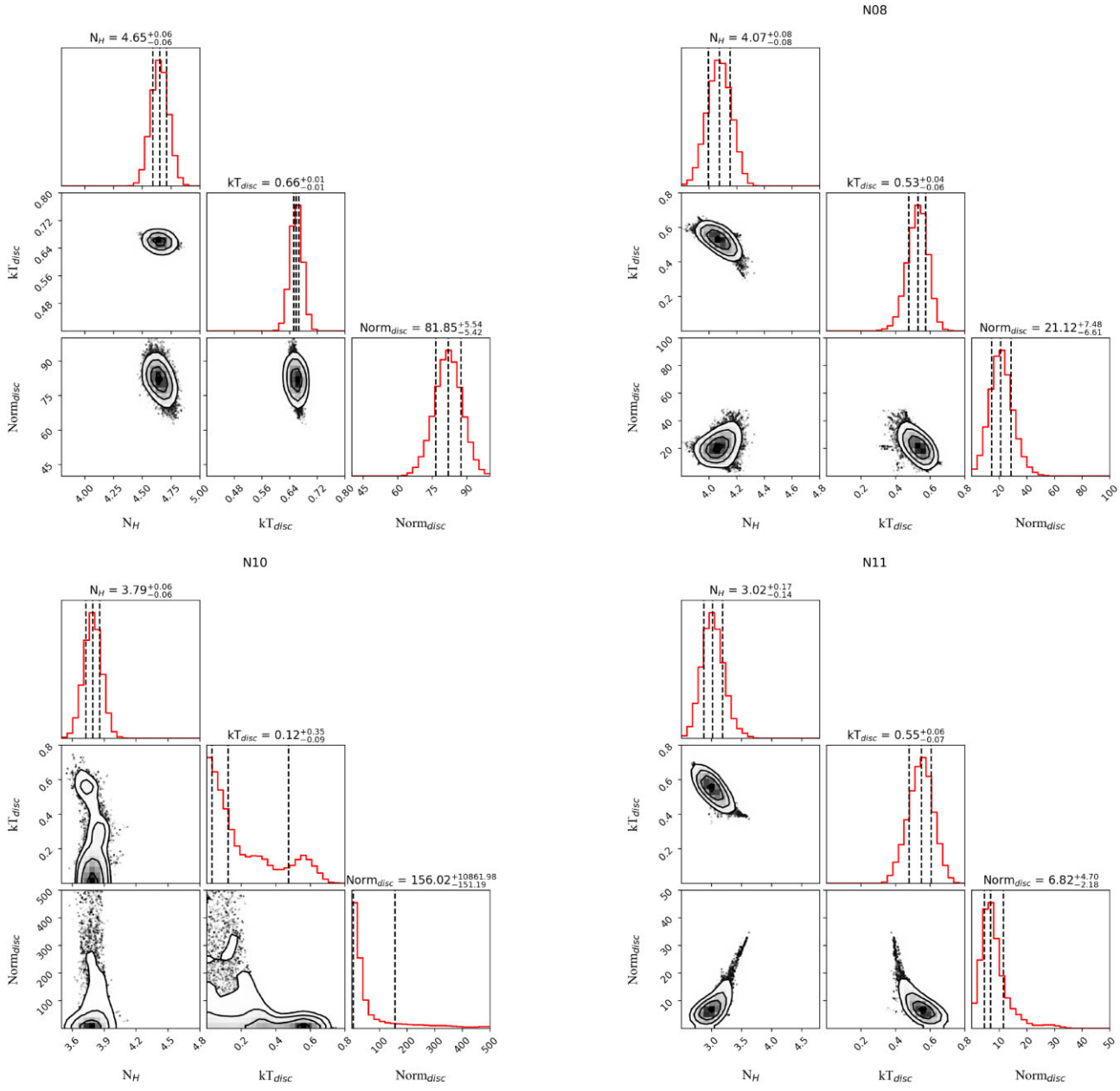

Figure 7. Posterior probability distributions for N_H, $kT_{\rm bb}$ and the `bbodyrad` normalization $\rm Norm_{bb}$. Contours represent the 1σ, 2σ, and 3σ confidence levels. Marginal posterior distributions are shown as histograms with the median and 1σ intervals of confidence highlighted as dashed lines.

If disc truncation is a consequence of the NS dipolar magnetic field halting the accretion flow, the inner edge of the disc obtained from reflection must coincide with such magnetospheric radius, i.e. the distance where the magnetospheric pressure R_m (Ghosh & Lamb 1979) equals the ram pressure of the accreted matter. In order to test this scenario, we solved the following formula (Frank, King & Raine 2002):

$$R_m = \phi \times 2.9 \times 10^8 L_{37}^{-2/7} M_{1.4}^{1/7} R_6^{-2/7} \mu_{30}^{4/7} \text{ cm}, \quad (1)$$

where ϕ is a factor of order 0.3–0.5 (Burderi & King 1998) that accounts for disc-fed accretion flows, L_{37} is the bolometric luminosity in 10^{37} erg s^{-1} units, $M_{1.4}$ the NS mass in 1.4 $M_\odot$ units, R_6 the NS radius in 10^6 cm units, and μ_{30} (equal to BR^3) is the magnetic dipole momentum in units of 10^{30} G cm^3. By assuming $M_{1.5} = 1, R_6 = 1$, and $R_m = R_{\rm in}$, we solved for B and found that to justify the truncation radius obtained from reflection, the magnetic field must be comprised between 0.9×10^9 G and 3.0×10^9 G, corresponding to $\phi = 0.5$. The obtained result is in line with the upper limits obtained for several AMXPs (e.g. Mukherjee et al. 2015) but almost an order of magnitude higher with respect to the upper limit on the magnetic field measured from the long-term NS spin evolution in the same source, i.e. $B < 1.3 \times 10^8$ G (Sanna et al. 2022). The discrepancy may indicate that the disc is not truncated by the magnetospheric pressure and that other mechanisms are responsible for halting the disc, e.g. the accretion flow becomes radiatively inefficient beyond such radius as typically observed in black hole XRBs at low luminosities. It is also noteworthy that the reflecting region may not necessarily coincide with the real inner edge of the accretion disc, for example if some self-shielding effects are at play, so that the latter may not coincide with the measure of $R_{\rm in}$ obtained in this analysis.

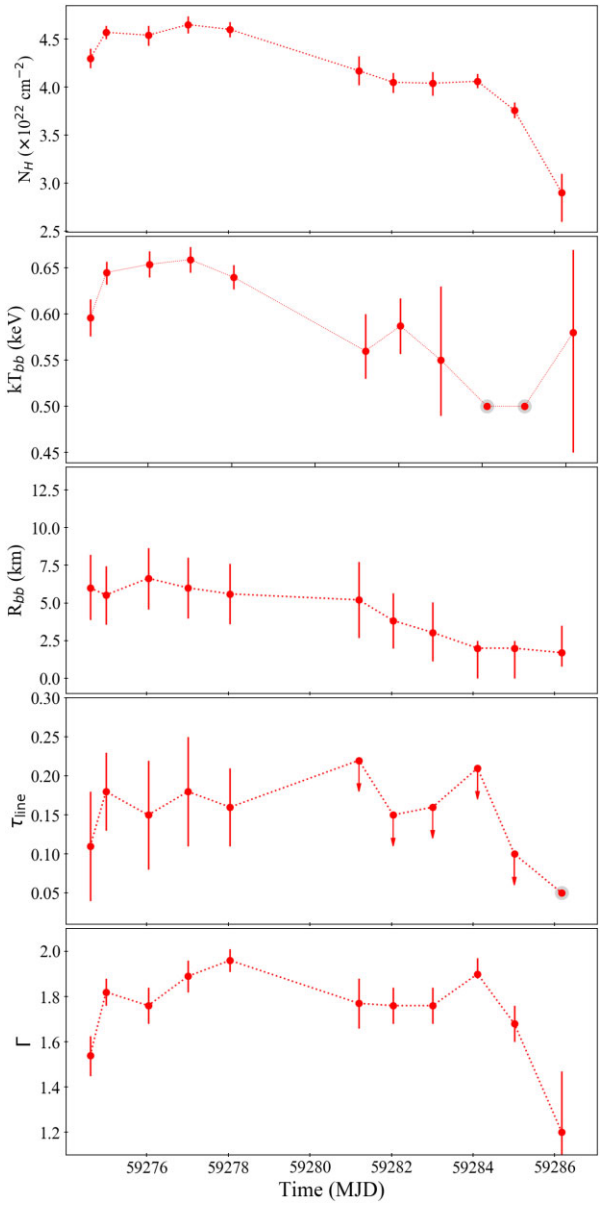

Figure 8. Evolution of the best-fit parameters for $N_{\rm H}$, $kT_{\rm bb}$, $R_{\rm bb}$, $\tau_{\rm line}$, and Γ over the eleven analysed epochs. Upper (lower) limits are represented with arrows. When corresponding to parameters that were kept frozen, the data points are represented with a grey exterior outer circle.

4.2 On the identification of the spectral state

When observed in an outburst, AMXPs are typically hard and rarely display a transition to the soft state (Di Salvo & Sanna 2022). This behaviour is not found in most (persistent or transient) atolls (Hasinger & van der Klis 1989), which show a variety of states, from hard to soft, characterized by different spectral and timing properties. In SWIFT J1749.4–2807 , the HR remains quite high, i.e. about 3–5, for the whole outburst, suggesting a behaviour similar to the other AMXPs. Furthermore, the spectral continuum is clearly never dominated by the disc and/or the NS thermal components, as expected instead for soft states. The electron temperature of the corona found in the Epoch 4, the only one for which we have broad-band spectral coverage, i.e. 12–14 keV, is also comparable with the temperature found for other NS LMXBs in hard-intermediate

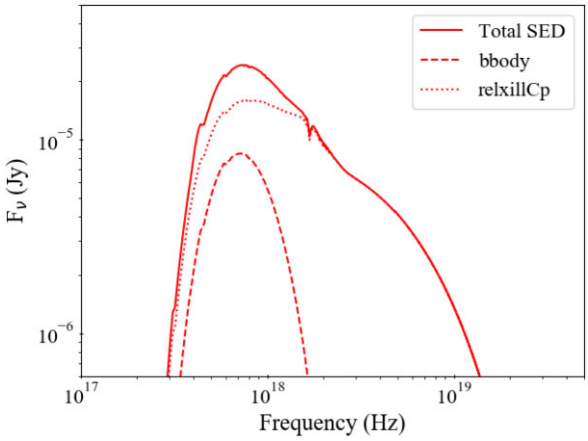

Figure 9. SWIFT J1749.4–2807 spectral energy distribution in Epoch 4, determined with the best-fitting parameters reported in Table 2. The single spectral components are highlighted with different line styles.

states (e.g. Pintore et al. 2018; Marino et al. 2019a). It is noteworthy that the the spectral energy distribution (SED) for Epoch 4 (Fig. 9) appears similar to the SED found in other NS LMXBs in hard state (e.g. Bianchi et al. 2017; Ponti et al. 2019), in particular considering the spectral cut-off energy, i.e. beyond 10^{19} Hz. Such a comparison is quite intriguing, since those authors found that winds were absent in the observations characterized by such hard SEDs but were present instead in softer states. However, the timing properties of SWIFT J1749.4–2807 would be more reminiscent of a soft state and somehow contradict the hard state identification. NS LMXBs in hard state display typical values of *rms* amplitude of about 10–20 per cent or higher (see e.g. Muñoz-Darias et al. 2014), while SWIFT J1749.4–2807 seems to show very little variability (*rms* of about 6 per cent). It is noteworthy that such a lack of variability characterizes all *NICER* observations, also the ones taken at the end of the outburst, where the HR increase and the Γ decreasing trends would suggest a hardening. This points out that the timing properties of the system are rather anomalous. However, a comprehensive study on the origin of such weak variability goes beyond the scope of the paper. Finally, we note that the difficulty in detecting any power in the PDS could be partly due to *NICER* being most sensitive at low energies, where low X-ray variability is expected.

4.3 Detection of disc winds out of a canonical soft state

The detection of an absorption blue-shifted Fe XXVI line at ∼7.0 keV indicates the presence of a disc wind in the outburst. According to the estimated outflow velocity, matter is ejected at 600–2700 km s^{-1} (∼0.002–0.007 c). The feature was also found in 6 out of 11 single *NICER* observations, although statistics in those spectra is too low to find any constraints on the centroid energy and its width. No trace of similar structures could be spotted in the residuals of the remaining five spectra and we were able only to estimate upper limits on the absorption strength and on the equivalent width (upper limit of about 0.02 keV or lower in all observations). In order to establish whether the disappearance of the absorption line was intrinsic or due to the lower statistics, we summed these five spectra together, finding that the feature was absent also in such joint spectrum. Only upper limits could be estimated for the absorption strength of such feature, corresponding to $\tau_{\rm line}$<0.04, and to the equivalent width, lower than 0.02 keV also in this case. Such test points out that the outflow could be active only during the peak of the outburst. Indeed, the

further hardening of the continuum in the final stages of the outburst, witnessed e.g. by a generally decreasing Γ in Table 3, could make the wind unstable and be responsible for its disappearance (see e.g. Chakravorty, Lee & Neilsen 2013; Higginbottom et al. 2020; Petrucci et al. 2021).

Disc winds are commonly observed in XRBs viewed at high inclination harbouring both black holes (BHs, see e.g. Ponti et al. 2012) and NSs (see e.g. D'Aì et al. 2014; Pintore et al. 2014), with orbital periods typically large, i.e. ∼hours (Díaz Trigo & Boirin 2016). According to the standard observational picture in BH systems (see e.g. Miller et al. 2008), winds are typically observed only during soft states, while matter ejection in hard state occurs mainly in the form of compact jets (but see, Homan et al. 2016, for a critical discussion on jet-winds mutual exclusion). The detection of winds only in the soft states of the NS LMXBs EXO 0748–676 (Ponti et al. 2014) and AX J1745.6–2901 (Ponti et al. 2015) suggest a similar pattern for NS systems. However, in the last few years, the detection of optical/UV winds in several transient systems during their hard state, e.g. in the BH LMXBs MAXI J1820 + 070 (Muñoz-Darias et al. 2019), MAXI J1803-298 (Mata Sánchez et al. 2022), and recently in the NS XRB Swift J1858.6–0814 (Castro Segura et al. 2022), has complicated the picture, revealing that outflow signatures in the optical/UV band may be common features in XRBs in hard states. AMXPs pose further challenges to our understanding of when and where disc winds are expected, as several claims for Doppler-shifted absorption features in the X-ray band have been put forward. The discovery of a Doppler-shifted Si XIII line at ∼1.9 keV has been firmly detected in IGR J17591–2342 (Nowak et al. 2019) and interpreted as the signature of disc winds at ∼0.1 c. Weak detections of outflows have been reported also in two other AMXPs (van den Eijnden et al. 2018; Di Salvo et al. 2019), which, if confirmed, would also imply the existence of winds in systems with orbital periods lower than 2 h. The discovery of a weakly relativistic equatorial wind in SWIFT J1749.4–2807 may represent another clear exception to the aforementioned winds paradigm. Winds are indeed present in an observation which, based on the spectral characteristics, would be more consistent with an intermediate or hard-intermediate state (see Section 4.2). Concerning the origin of such outflow, among the three physical mechanisms typically invoked for winds, i.e. thermally driven, magnetically driven, and radiation pressure-driven (see e.g. Díaz Trigo & Boirin 2016, and references therein), the latter cannot hold in the present case as it would require Eddington or super-Eddington luminosities (Proga & Kallman 2002), unless the intrinsic luminosity in the system is higher and scattering from the surrounding material makes it look fainter (as in the case of 4U 1822–37, see e.g. Anitra et al. 2021). In order to distinguish between thermally and magnetically driven winds, the radius of wind launching should be constrained, since thermal winds are expected to arise from the outermost part of large discs, i.e. where the sound speed of the plasma overcomes the Keplerian speed (see e.g. Higginbottom et al. 2017). It is noteworthy that in magnetized NSs, winds could also be in principle propeller-driven, i.e. launched when the magnetic field is rotating faster than the accretion flow creates a centrifugal barrier able to sweep matter away (e.g. Illarionov & Sunyaev 1975; Romanova et al. 2009). As already discussed in Section 4.1, the high truncation radius obtained from reflection could be ascribed to the magnetospheric pressure dominating over ram pressure at such distance and this, in turn, could be responsible for wind launching in this particular case. The onset of propellers require a dipole magnetic field interacting with the accretion flow and a relatively weak accretion rate, both ingredients typically present in AMXPs, but absent in BH LMXBs and in the other, non-pulsating NS LMXBs (where the magnetic field could be buried inside the NS) as well, and could constitute an explanation for observing disc winds even outside of the spectral soft state.

Along with the evidence of a wind, we also included a model describing absorption by ionized material, i.e. ZXIPCF, but only in the broad-band spectrum the parameters of the model could be constrained. According to the obtained best-fitting parameters, such material covers only ∼10 per cent of the background illuminating X-ray source and it has high-column density ($N_{H,\,IA} \gtrsim 2.9 \times 10^{24}$ cm^{-2}) and high-ionization state ($\log \xi_{IA} \sim 3.1 - 4.4$). According to the low covering fraction found, this absorbing material could be interpreted as an ionized layer of plasma coating the optically thick disc and seen edge-on, most likely associated with the Fe XXVI wind. It is noteworthy that with such a high-column density, absorption features produced by lower Z species should appear at soft X-rays, but this effect is masked by the large neutral column density $N_{\rm H}$ due to interstellar absorption. Furthermore, the highly dense local ionized absorber could also produce significant Thomson scattering, which in turn would reduce the X-ray luminosity and in principle explain the faintness of the system. Unfortunately, the parameters of the model in the single *NICER* spectra were too unconstrained to check for an evolution of such absorbing material along with the outburst decay.

4.4 Outflows and non-conservative mass-transfer

Matter eruption in the form of winds is able in principle to remove a significant amount of mass from the system. The mass-loss rate due to winds, $\dot{M}_w$, can be indeed expressed as (Ponti et al. 2012, 2015):

$$\dot{M}_w = 4\pi m_p v_{\rm out} \frac{L_X}{\xi} \frac{\Omega}{4\pi}, \quad (2)$$

with m_p the proton mass, $v_{\rm out}$ and ξ the velocity and the ionization of the outflowing plasma, respectively, and Ω the solid angle subtended by the wind. Since we do not detect spectral signatures of Fe XXV or other less-ionized species of iron, the plasma is most likely highly ionized and we assume ξ to be 10^4, in accordance with the ion distributions computed by Kallman & Bautista (2001) and the values obtained for the ionization of the absorber with ZXIPCF. In order to calculate Ω, we considered two cases: we first assumed a wind opening angle of 30° (as in e.g. Ponti et al. 2012) or 10°, the latter under the hypothesis that the wind and the ionized material (covering about 10 per cent of the X-ray source, see Section 3.1), are associated with each other. Finally, at the outburst peak, i.e. from the analysis of the broad-band spectrum, we estimated v_{out} in the range 600–2700 km s^{-1} and a bolometric X-ray luminosity of $\sim 7 \times 10^{36}$ erg s^{-1}, which corresponds to a $\dot{M}_w$ of 0.6–2.7 $\times$ 10^{17} g s^{-1} for $\Omega = 30°$ and 0.7–3 $\times$ 10^{16} g s^{-1} for $\Omega = 10°$. Now, considering that the mass-accretion rate $\dot{M}_2$ and L_X are connected by the relation $L_X = \frac{GM_1\dot{M}_2}{R_1}$, with M_1 and R NS mass and radius and assuming a NS mass of 1.5 M$_\odot$ and radius of 12 km (values commonly found for NSs, see Özel & Freire 2016, for a review), we estimated the rate of mass inflow at the outburst peak to be about $\sim 4 \times 10^{17}$ g s^{-1}. It follows that, for $\Omega\,\dot{M}_w \sim 0.15 - 0.70\dot{M}_2$, i.e. the rate of mass outflows due to winds is almost comparable to the rate of mass inflow. The overall mass-transfer regime results to be therefore definitely non-conservative.

A highly non-conservative mass-transfer (NCMT) regime[7] has been invoked in the past to explain the strong orbital expansion rates, too strong to be explained with angular momentum losses

[7]But see also Applegate & Shaham (1994) for an alternative theory.

via gravitational radiation (GR) or magnetic braking, observed in (almost) all the AMXPs observed more than once in outburst (Di Salvo et al. 2008; Burderi et al. 2009; Mukherjee et al. 2015; Sanna et al. 2018b; Bult et al. 2021a). According to the orbital period derivative of SWIFT J1749.4–2807, measured after the outburst analysed here, the system is rapidly expanding as well, and also in this case such phenomenon could imply a NCMT (Sanna et al. 2022). A high rate of mass-loss was also implied by multiwavelength modelling of IGR J17062–6143 (Hernández Santisteban et al. 2019), somehow giving indirect evidence for the outflow claimed by van den Eijnden et al. (2018). The (unexpected) presence of winds (see Section 4.3 and references therein) and the evidence that AMXPs appear more radio bright than the other non-pulsating NS LMXBs, i.e. they exhibit stronger ejections in the form of jets (e.g. Tetarenko et al. 2016; Russell et al. 2018), corroborate a scenario where AMXPs are very efficient engines when it comes to ejection of significant amounts of the mass transferred by the companion.

Indirect evidences for a NCMT scenario in almost half of the AMXPs known so far have been found from the comparison between the energy output expected in the conservative case, i.e. where all the transferred mass is effectively accreted on to the NS surface, and the energy output actually observed. Such a methodology was developed in Marino et al. (2017) and then applied to the large majority of the known AMXPs in Marino et al. (2019b). These authors obtained strong indications for a NCMT in five systems in the sample, including SWIFT J1749.4–2807. In this paragraph, we apply this method again to our system, including three additional years of quiescence and the 2021 outburst, analysed in this manuscript. Broadly speaking (see Marino et al. 2019b, for a detailed description of the method and discussion of the main caveats), the method consists of comparing the total amount of energy emitted by the system $E_{\rm tot,\,exp}$ expected in the case of a fully conservative mass-transfer with the observed energy output $E_{\rm tot,\,obs}$ measured during each outburst displayed by the system since 1996.[8] Considering that the expected luminosity $L_{\rm exp}$ can be expressed as $L_{\rm exp} = \dfrac{GM_1\dot{M}_2}{R}$, with M_1 and R NS mass and radius and $\dot{M}_2$ the mass-transfer rate, $L_{\rm exp}$ was obtained by adopting $M_1 = 1.5\,{\rm M}_\odot$ and $R_1 = 12$ km. In order to compute $\dot{M}_2$, we solved equations (2) and (3) of Marino et al. (2019b), using for M_2 the value derived from the mass function $f = 0.055$ by fixing the inclination to the known value of 77° (Altamirano et al. 2011) and considering only angular momentum losses via GR. The total expected energy output $E_{\rm tot,\,exp}$ can be obtained by simply multiplying $L_{\rm exp}$ by the chosen baseline, i.e. the 25 yr period between 1996 and 2021, and it equals $E_{\rm tot,\,exp} = 1.3 \times 10^{44}$ ergs. Concerning the observed energy output $E_{\rm tot,\,obs}$, for both the 2010 outburst (see Marino et al. 2019b, for more details) and the 2021 outburst analysed here, we estimated the fluence (ϕ_{2010} and ϕ_{2021}) as the area subtended by the X-ray light curve of each outburst and extended this value in the range 0.5–300 keV. By taking 6.7 kpc as the distance of the system, the value of $E_{\rm tot,\,obs}$ is obtained by scaling the fluence for the area over which such fluence spreads before reaching the observer, i.e. $E_{\rm tot,\,obs} = (\phi_{2010} + \phi_{2021}) \times 4\pi d^2$. The observed energy output results therefore equal to $\sim 1.5 \times 10^{43}$, i.e. one order of magnitude below the expected energy for a conservative scenario. Even considering the contribution of the energy emitted during quiescence, at an average X-ray luminosity of 10^{33}-10^{34} erg s^{-1}, the two values could not be reconciled and, unless we missed one or more outburst during the time taken into account, the previous claim that the system is undergoing a NCMT scenario (Marino et al. 2019b) is confirmed. We also notice that the companion star in SWIFT J1749.4–2807 is not a degenerate helium dwarf or a white dwarf, so that the effects of magnetic braking should be included. Considering this additional angular momentum loss channel would make the expected luminosity even higher, so that the value obtained for $E_{\rm out,\,exp}$ has to be considered a lower limit.

Whether or not the disc winds found in this work could be entirely responsible for the discrepancy between expected and observed luminosity discussed above and the high orbital period derivative measured in the system (Sanna et al. 2022), it is unclear. In order to investigate such connection, we should know how much angular momentum winds extract from the system, i.e. the location from where winds are launched, and we should have estimates of $\dot{M}_w$ for the whole outburst, not only at the peak. It is also most likely that the NCMT observed results from several channels of mass-loss other than winds, such as the removal of matter during quiescence due to pulsar winds (see e.g. Burderi et al. 2001; Parfrey & Tchekhovskoy 2017) and jets.

4.5 The end of the outburst: dawn of a power-law quiescence spectrum?

In Section 3.3, we showed that, past the outburst peak, N_H decreases significantly, the hotspot shrinks, going from 6 to 2 km radii, and the continuum hardens. A scenario with variable N_H can be explained by invoking changes over short time-scales of local, neutral absorption in the system. Concerning the decreasing trend in the blackbody radius, several mechanisms may be invoked to explain it. It is plausible that the decrease in mass-accretion rate throughout the outburst implies a progressively smaller amount of energy supplied to the polar caps through the magnetic field lines. Along with the energy, we suggest that the area over which this energy is distributed may decrease as well. A similar reduction in the hotspot size at the end of the outburst could be a consequence of the disc being truncated further away, e.g. due to the reduced mass-accretion rate. Indeed, as the material moves outwards, it pulls away the coupled magnetic field lines, forcing their footprints on the neutron star surface to move inwards and thereby reducing the hotspot perimeter. However, whether such an evolution is compatible with the increase of the pulsed fraction in the final stages of the outburst is yet to be established (Sanna et al. 2022).

Unfortunately, the lack of data at soft X-rays taken during the (relatively unexplored) termination of XRB outbursts makes drawing comparisons with analogous similar sources quite challenging. However, it is noteworthy that in the 'very faint', i.e. 10^{34}–10^{36} erg s^{-1}, and quiescence, below 10^{34} erg s^{-1}, luminosity ranges, AMXPs tend to show somehow harder spectra (with some exceptions, e.g. Ng et al. 2021), i.e. typically dominated by power-law like spectral components, with respect to other NS LMXBs (see e.g. Campana et al. 2005; Degenaar et al. 2012; Linares et al. 2014; Wijnands et al. 2015, and references therein). The origin of this power-law shaped spectrum in quiescence has been ascribed to residual accretion or physical processes related to the NS magnetic field (e.g. Fridriksson et al. 2011; Chakrabarty et al. 2014; Parikh et al. 2017). This occurs in striking contrast with respect to a large number of NS LMXBs, typically non-magnetized, which show purely soft, quasi-thermal spectra, due to the slow release of the energy stored in the crust when accretion was ongoing (see e.g. Brown & Bildsten 1998; Degenaar et al. 2011; Servillat et al. 2012; Marino et al. 2018). When observed in quiescence in 2011, SWIFT J1749.4–2807 X-

[8] Since 1996, the X-ray sky has almost continuously monitored, so that we had good chances of recording any outburst from an AMXP.

ray spectrum was found to be well-described with a simple power-law model (Degenaar et al. 2012), without any contribution by a thermal component. It is therefore plausible that the hardening of the spectrum and the shrinking of the hotspot at the end of the outburst in SWIFT J1749.4–2807 witness the dawn of a power-law dominated quiescence spectrum. Future observations of the system in quiescence are necessary to confirm this hint.

5 CONCLUSIONS

In this manuscript, we investigated the X-ray emission of the AMXP SWIFT J1749.4–2807 during its short and rather dim outburst that occurred in 2021. Exploiting data from *XMM-Newton*, *NuSTAR*, and *NICER* at the outburst peak and from *NICER* in the whole outburst, we were able to characterize the geometry of the accretion flow and the main physical parameters of the system to scrutinize their evolution from rise to decay.

In the following, we summarize the main findings of our work:

(i) Throughout the outburst, the spectrum can be described by the sum of a blackbody component, likely due to a hotspot on the NS surface, and a Comptonization spectrum that can be associated with a hot corona scattering off photons from a cold disc, whose direct emission is likely too faint for detection;

(ii) From the analysis of the reflection component, we estimated the radius of the accretion disc to be about 20–34 R_G (40–68 km). A magnetic field strength of at least 9×10^8 G would be required if this radius coincides with the magnetospheric radius, i.e. the interruption of the disc is caused by the magnetospheric pressure taking over.

(iii) A blue-shifted Fe XXVI line was found in absorption in the broad-band spectrum and in 6 out of 11 *NICER* spectra. The presence of this feature witnesses the presence of a mildly relativistic equatorial disc wind, at a velocity of about 0.2–0.7 per cent c. Despite winds being typically thought to be present in soft states only, we point out that the detection of these outflows in a number of AMXPs, including SWIFT J1749.4–2807 , could suggest a different launching mechanism, e.g. a propeller-driven wind.

(iv) An additional spectral component, taking into account absorption from an ionized plasma, is required by the fit. As such plasma covers only 10 per cent of the source, it is compatible with a thin layer of ionized plasma coating the disc, most likely associated with the detected disc wind.

(v) We were able to follow the evolution of the hotspot on the NS surface until the end of the outburst and observed it cooling down and shrinking down to a size of $\sim$2 km^2 as it faded to quiescence. This may be consistent with the quiescence spectrum of the system being a pure power-law spectrum, with negligible contribution from the NS surface.

(vi) Following Marino et al. (2019b), where a method to check whether the mass-transfer in a LMXB is conservative or non-conservative was developed and applied to a sample of 19 AMXPs, we updated the results obtained for SWIFT J1749.4–2807, including the outburst analysed in this paper. Although the discrepancy between expected average luminosity for a conservative mass-transfer and the observed one is lower than in our previous work, it is still quite large and confirms that SWIFT J1749.4–2807 loses a significant fraction of the mass transferred by the companion.

Despite many outbursts being surveyed in detail in the *RXTE* era, with *NICER* we have the unprecedented opportunity to follow how the system evolves in the soft X-ray band, which permits accessing e.g. the details of the blackbody emission. Furthermore, thanks to *NICER* sensitivity and flexibility, we were able to follow the whole outburst until its transition to quiescence, when the system enters in a faint and relatively poorly explored flux regime (i.e. below 10^{36} erg s^{-1}). Further studies of this and/or analogous objects will give the opportunity to investigate the behaviour of accreting NSs at low Eddington rates and the critical role of matter outflows in such states.

ACKNOWLEDGEMENTS

We would like to thank the anonymous referee for their useful comments. AM acknowledges a financial contribution from the agreement ASI-INAF n.2017-14-H.0 and the INAF mainstream grant (PI: T. Belloni, A. De Rosa). AM, TDS, AA, and RI acknowledge financial contribution from the HERMES project financed by the Italian Space Agency (ASI) Agreement n.2016/13 U.O. AM is supported by the H2020 ERC Consolidator Grant 'MAGNESIA' under grant agreement No. 817661 (PI: Rea) and National Spanish grant PGC2018-095512-BI00. This work was also partially supported by the program Unidad de Excelencia Maria de Maeztu CEX2020-001058-M and the PHAROS COST Action (No. CA16214). PB acknowledges support from the CRESST II cooperative agreement (80GSFC21M0002). SG acknowledges the support of the Centre National d'Etudes Spatiales (CNES). GCM was partially supported by Proyecto de Investigación Plurianual (PIP) 0102 (Consejo Nacional de Investigaciones Científicas y Técnicas (CONICET)) and PICT-2017-2865 (Agencia Nacional de Promoción Científica y Tecnológica (ANPCyT)). DA acknowledges support from the Royal Society.

DATA AVAILABILITY

The data utilized in this article are publicly available at https://heasarc.gsfc.nasa.gov/cgi-bin/W3Browse/w3browse.pl, while the analysis products will be shared on reasonable request to the corresponding author.

REFERENCES

Altamirano D. et al., 2011, ApJ, 727, L18
Anitra A. et al., 2021, A&A, 654, A160
Applegate J. H., Shaham J., 1994, ApJ, 436, 312
Archibald A. M. et al., 2009, Science, 324, 1411
Archibald A. M., Kaspi V. M., Hessels J. W. T., Stappers B., Janssen G., Lyne A., 2013, preprint (arXiv:1311.5161)
Bahramian A. et al., 2021, MNRAS, 501, 2790
Bassa C. G. et al., 2014, MNRAS, 441, 1825
Belloni T., 2010, The Jet Paradigm, 794, 285
Bianchi S., Ponti G., Muñoz-Darias T., Petrucci P.-O., 2017, MNRAS, 472, 2454
Bradt H. V., Rothschild R. E., Swank J. H., 1993, A&AS, 97, 355
Brown E. F., Bildsten L .&Rutledge R.,1998, ApJ, 504, L95–L9
Bult P., Chakrabarty D., Arzoumanian Z., Gendreau K. C., Guillot S., Malacaria C., Ray P. S., Strohmayer T. E., 2020, ApJ, 898, 38
Bult P., Strohmayer T. E., Malacaria C., Ng M., Wadiasingh Z., 2021a, ApJ, 912, 120
Bult P. M. et al., 2021b, Astron. Telegram, 14428, 1
Bult P. M. et al., 2022, Astron. Telegram, 15425, 1
Burderi L., King A. R., 1998, ApJ, 505, L135
Burderi L. et al., 2001, ApJ, 560, L71
Burderi L., Riggio A., di Salvo T., Papitto A., Menna M. T., D'Aì A., Iaria R., 2009, A&A, 496, L17
Campana S., 2009, ApJ, 699, 1144

Campana S., Di Salvo T., 2018, The Physics and Astrophysics of Neutron Stars, Astrophysics and Space Science Library, Vol. 457 , Springer Nature Switzerland AG, p. 149
Campana S., Ferrari N., Stella L., Israel G. L., 2005, A&A, 434, L9
Castro Segura N. et al., 2022, Nature, 603, 52
Chakrabarty D. et al., 2014, ApJ, 797, 92
Chakravorty S., Lee J. C., Neilsen J., 2013, MNRAS, 436, 560
Cocchi M., Bazzano A., Natalucci L., Ubertini P., Heise J., Kuulkers E., Cornelisse R., in't Zand J. J. M., 2001, A&A, 378, L37
Cornelisse R. et al., 2002, A&A, 392, 885
D'Aì A. et al., 2010, A&A, 516, A36
D'Aì A., Iaria R., Di Salvo T., Riggio A., Burderi L., Robba N. R., 2014, A&A, 564, A62
D'Avanzo P., Campana S., Muñoz-Darias T., Belloni T., Bozzo E., Falanga M., Stella L., 2011, A&A, 534, A92
Dauser T., Garcia J., Wilms J., Böck M., Brenneman L. W., Falanga M., Fukumura K., Reynolds C. S., 2013, MNRAS, 430, 1694
Degenaar N. et al., 2011, MNRAS, 412, 1409
Degenaar N., Patruno A., Wijnands R., 2012, ApJ, 756, 148
Degenaar N., Pinto C., Miller J. M., Wijnands R., Altamirano D., Paerels F., Fabian A. C., Chakrabarty D., 2017, MNRAS, 464, 398
Del Santo M., Sidoli L., Mereghetti S., Bazzano A., Tarana A., Ubertini P., 2007, A&A, 468, L17
Del Santo M., Sidoli L., Romano P., Bazzano A., Wijnands R., Degenaar N., Mereghetti S., 2010, MNRAS, 403, L89
de Martino D. et al., 2013, A&A, 550, A89
den Herder J. W. et al., 2001, A&A, 365, L7
Di Salvo T., Sanna A., 2022, Millisecond Pulsars, Springer International Publishing, p. 87
Di Salvo T., Burderi L., Riggio A., Papitto A., Menna M. T., 2008, MNRAS, 389, 1851
Di Salvo T., Sanna A., Burderi L., Papitto A., Iaria R., Gambino A. F., Riggio A., 2019, MNRAS, 483, 767
Díaz Trigo M., Boirin L., 2016, Astron. Nachr., 337, 368
Done C., Gierliński M., Kubota A., 2007, A&AR, 15, 1
Egron E. et al., 2013, A&A, 550, A5
Fabian A. C., Rees M. J., Stella L., White N. E., 1989, MNRAS, 238, 729
Falanga M. et al., 2005, A&A, 436, 647
Ferrigno C. et al., 2011, A&A, 525, A48
Foreman-Mackey D., 2016, J. Open Source Softw., 1, 24
Frank J., King A., Raine D. J., 2002, Accretion Power in Astrophysics: Third Edition,Cambridge University Press,,Cambridge, UK, p. 398
Fridriksson J. K. et al., 2011, ApJ, 736, 162
García J. et al., 2014, ApJ, 782, 76
Ghosh P., Lamb F. K., 1979, ApJ, 234, 296
Gierliński M., Done C., 2002, MNRAS, 337, 1373
Gierliński M., Zdziarski A. A., Poutanen J., Coppi P. S., Ebisawa K., Johnson W. N., 1999, MNRAS, 309, 496
Goodman J., Weare J., 2010, Commun. Appl. Math. Comput. Sci., 5, 65
Hasinger G., van der Klis M., 1989, A&A, 225, 79
Heinke C. O., Bahramian A., Degenaar N., Wijnands R., 2015, MNRAS, 447, 3034
Hernández Santisteban J. V. et al., 2019, MNRAS, 488, 4596
Higginbottom N., Proga D., Knigge C., Long K. S., 2017, ApJ, 836, 42
Higginbottom N., Knigge C., Sim S. A., Long K. S., Matthews J. H., Hewitt H. A., Parkinson E. J., Mangham S. W., 2020, MNRAS, 492, 5271
Homan J., Neilsen J., Allen J. L., Chakrabarty D., Fender R., Fridriksson J. K., Remillard R. A., Schulz N., 2016, ApJ, 830, L5
Iaria R., Mazzola S. M., Di Salvo T., Marino A., Gambino A. F., Sanna A., Riggio A., Burderi L., 2020, A&A, 635, A209
Illarionov A. F., Sunyaev R. A., 1975, A&A, 39, 185
in't Zand J. J. M., Jonker P. G., Bassa C. G., Markwardt C. B., Levine A. M., 2009, A&A, 506, 857
Kaastra J. S., Bleeker J. A. M., 2016, A&A, 587, A151
Kallman T., Bautista M., 2001, ApJS, 133, 221
King A. R., Wijnands R., 2006, MNRAS, 366, L31
Kubota A., Tanaka Y., Makishima K., Ueda Y., Dotani T., Inoue H., Yamaoka K., 1998, PASJ, 50, 667
Linares M. et al., 2014, MNRAS, 438, 251
Madsen K. K., Grefenstette B. W., Pike S., Miyasaka H., Brightman M., Forster K., Harrison F. A., 2020, preprint (arXiv:2005.00569)
Marino A., Di Salvo T., Gambino A. F., Iaria R., Burderi L., Matranga M., Sanna A., Riggio A., 2017, A&A, 603, A137
Marino A., Degenaar N., Di Salvo T., Wijnands R., Burderi L., Iaria R., 2018, MNRAS, 479, 3634
Marino A. et al., 2019a, MNRAS, 490, 2300
Marino A. et al., 2019b, A&A, 627, A125
Markwardt C. B., Strohmayer T. E., 2010, ApJ, 717, L149
Mata Sánchez D. et al., 2022, ApJ, 926, L10
Mereminskiy I. A., Grebenev S. A., Lutovinov A. A., Krivonos R. A., Kuulkers E., 2021, Astron. Telegram, 14427, 1
Miller J. M., 2007, ARA&A, 45, 441
Miller J. M. et al., 2003, ApJ, 583, L99
Miller J. M., Raymond J., Reynolds C. S., Fabian A. C., Kallman T. R., Homan J., 2008, ApJ, 680, 1359
Muñoz-Darias T., Fender R. P., Motta S. E., Belloni T. M., 2014, MNRAS, 443, 3270
Muñoz-Darias T. et al., 2019, ApJ, 879, L4
Mukherjee D., Bult P., van der Klis M., Bhattacharya D., 2015, MNRAS, 452, 3994
Muno M. P., Pfahl E., Baganoff F. K., Brandt W. N., Ghez A., Lu J., Morris M. R., 2005, ApJ, 622, L113
Ng M. et al., 2021, ApJ, 908, L15
Ng M. et al., 2022, Astron. Telegram, 15444, 1
Nowak M. A., Paizis A., Jaisawal G. K., Chenevez J., Chaty S., Fortin F., Rodriguez J., Wilms J., 2019, ApJ, 874, 69
Özel F., Freire P., 2016, ARA&A, 54, 401
Papitto A., de Martino D., 2022, Millisecond pulsars,Springer International Publishing, p. 157
Papitto A., Riggio A., di Salvo T., Burderi L., D'Aì A., Iaria R., Bozzo E., Menna M. T., 2010, MNRAS, 407, 2575
Papitto A. et al., 2013, MNRAS, 429, 3411
Papitto A., de Martino D., Belloni T. M., Burgay M., Pellizzoni A., Possenti A., Torres D. F., 2015, MNRAS, 449, L26
Papitto A. et al., 2019, ApJ, 882, 104
Parfrey K., Tchekhovskoy A., 2017, ApJ, 851, L34
Parikh A. S. et al., 2017, MNRAS, 466, 4074
Patruno A., 2012, ApJ, 753, L12
Patruno A., Watts A. L., 2021, Timing Neutron Stars: Pulsations, Oscillations and Explosions, Astrophysics and Space Science Library, Springer, Berlin Heidelberg, p. 143
Pavan L. et al., 2010, Astron. Telegram, 2548, 1
Petrucci P. O. et al., 2021, A&A, 649, A128
Pintore F. et al., 2014, MNRAS, 445, 3745
Pintore F. et al., 2016, MNRAS, 457, 2988
Pintore F. et al., 2018, MNRAS, 479, 4084
Ponti G., Fender R. P., Begelman M. C., Dunn R. J. H., Neilsen J., Coriat M., 2012, MNRAS, 422, L11
Ponti G., Muñoz-Darias T., Fender R. P., 2014, MNRAS, 444, 1829
Ponti G. et al., 2015, MNRAS, 446, 1536
Ponti G., Bianchi S., De Marco B., Bahramian A., Degenaar N., Heinke C. O., 2019, MNRAS, 487, 858
Proga D., Kallman T. R., 2002, ApJ, 565, 455
Reeves J., Done C., Pounds K., Terashima Y., Hayashida K., Anabuki N., Uchino M., Turner M., 2008, MNRAS, 385, L108
Romanova M. M., Ustyugova G. V., Koldoba A. V., Lovelace R. V. E., 2009, MNRAS, 399, 1802
Roming P. W. A. et al., 2009, ApJ, 690, 163
Russell T. D., Degenaar N., Wijnands R., van den Eijnden J., Gusinskaia N. V., Hessels J. W. T., Miller-Jones J. C. A., 2018, ApJ, 869, L16
Sanna A. et al., 2017a, MNRAS, 471, 463
Sanna A. et al., 2017b, A&A, 598, A34
Sanna A. et al., 2018a, A&A, 610, L2
Sanna A. et al., 2018b, A&A, 616, L17
Sanna A. et al., 2022, MNRAS, 514, 4385

Schady P., Beardmore A. P., Marshall F. E., Palmer D. M., Rol E., Sato G., 2006, GRB Coord. Netw., 5200, 1
Servillat M., Heinke C. O., Ho W. C. G., Grindlay J. E., Hong J., van den Berg M., Bogdanov S., 2012, MNRAS, 423, 1556
Strohmayer T. E., Markwardt C. B., 2010, Astron. Telegram, 2569, 1
Strüder L. et al., 2001, A&A, 365, L18
Tetarenko A. J. et al., 2016, MNRAS, 460, 345
Turner M. J. L. et al., 2001, A&A, 365, L27
Verner D. A., Ferland G. J., Korista K. T., Yakovlev D. G., 1996, ApJ, 465, 487
van den Eijnden J., Bagnoli T., Degenaar N., Lohfink A. M., Parker M. L., in 't Zand J. J. M., Fabian A. C., 2017, MNRAS, 466, L98
van den Eijnden J. et al., 2018, MNRAS, 475, 2027
Wijnands R., van der Klis M., 1998, Nature, 394, 344
Wijnands R. et al., 2006, A&A, 449, 1117
Wijnands R., Rol E., Cackett E., Starling R. L. C., Remillard R. A., 2009, MNRAS, 393, 126
Wijnands R., Degenaar N., Armas Padilla M., Altamirano D., Cavecchi Y., Linares M., Bahramian A., Heinke C. O., 2015, MNRAS, 454, 1371
Wilms J., Allen A., McCray R., 2000, ApJ, 542, 914
Winkler C. et al., 2003, A&A, 411, L1

This paper has been typeset from a TEX/LATEX file prepared by the author.